Capacity-Fading Mechanisms of LiNiO$_2$-Based Lithium-Ion Batteries

II. Diagnostic Analysis by Electron Microscopy and Spectroscopy

Shunsuke Muto,[a,*,z] **Yusuke Sasano,**[a] **Kazuyoshi Tatsumi,**[a] **Tsuyoshi Sasaki,**[b,*]
Kayo Horibuchi,[b] **Yoji Takeuchi,**[b] **and Yoshio Ukyo**[b,*]

aDepartment of Materials, Physics and Energy Engineering, Graduate School of Engineering, Nagoya University, Nagoya 464-8603, Japan
bToyota Central Research and Development Laboratories, Incorporated, Nagoakute 480-1192, Japan

We used a suite of transmission electron microscopy (TEM) and associated electron spectroscopy methods to examine the local structure and changes in the electronic structure of LiNi$_{0.8}$Co$_{0.15}$Al$_{0.05}$O$_2$ positive electrode material. We found a scattered rock-salt phase near grain surfaces and grain boundaries, where Ni^{3+} turned to Ni^{2+}, deduced from relative intensity ratios and fine structures of the L$_{2,3}$ white-line peaks of the transition metals. The spatial distribution of the degraded phase throughout the secondary particle was found using a scanning TEM-electron energy loss spectroscopy spectral imaging technique and multivariate analysis. The degradation process and its relationship to the surface reactions with electrolytes is discussed based on the spatial-distribution map of the degraded phases.
© 2009 The Electrochemical Society.   [DOI: 10.1149/1.3076137] All rights reserved.

The class of oxides based on LiNiO$_2$ has been considered as a good replacement for LiCoO$_2$ in the positive electrode of advanced lithium-ion batteries because of its lower cost and higher capacity compared to LiCoO$_2$.[1] It has been demonstrated that partial substitution of Ni by Co and Al improves both thermal stability and cyclability.[2-6] The composition LiNi$_{0.8}$Co$_{0.15}$Al$_{0.05}$O$_2$, in which the performance of lithium-ion cells showed the most improvement, has been studied intensively. Unfortunately, battery cells using LiNi$_{0.8}$Co$_{0.15}$Al$_{0.05}$O$_2$ still showed capacity fading and resistance increase after charge/discharge test cycles at relatively high temperatures.[5,6] This degradation upon aging or charge/discharge cycling presents a significant barrier to high-power applications and has been found to be caused mainly by an increase in impedance at both positive and graphitic negative electrodes. Impedance measurements of the cell components suggested that the positive electrodes were primarily responsible for the observed loss of electrochemical performance.[7-10] Improvement of this class of batteries is now focused on when, where, and how this degradation of the positive electrodes occurs during aging.

While X-ray diffraction measurements have failed to detect any noticeable change in the bulk structure of positive electrodes,[6,11-13] X-ray absorption spectroscopy,[14] transmission electron microscopy (TEM), and associated spectroscopic methods have provided unique insight into the local chemical and structural changes that may be responsible for cell degradation.[15,16] The oxidation states of Ni and Co in the surface layer of LiNi$_{0.8}$Co$_{0.15}$Al$_{0.05}$O$_2$ composite were lower than those of the bulk, and the O-K-edge from the surface was typical of NiO. High-resolution TEM (HRTEM) images and nanoprobe diffraction patterns found a thin NiO-type surface layer on the LiNi$_{0.8}$Co$_{0.15}$Al$_{0.05}$O$_2$ particles, and the layer was thicker in the particles from the aged cell. In contrast, a previous report found no major new phases in TEM images of a sample after test cycles.[17] One possible reason for this discrepancy is that the quality and structure of the particles of active material may depend on the fabrication process or thin-foil preparation technique for TEM observation. Furthermore, HRTEM images and nanodiffraction patterns may not clearly reveal the superlattice reflections characteristic of the LiNi$_{0.8}$Co$_{0.15}$Al$_{0.05}$O$_2$ phase because of their lower intensities due to weak interaction between the structure and incident electrons at thin areas. It can therefore be difficult to distinguish between LiNiO$_2$-type and NiO-type structures, a task made still more challenging by the fact that both phases share a common geometry of

fundamental reflections or structural framework. It is hence desirable to carefully identify the secondary phase and its spatial distribution over wide areas of the primary particles with sufficient spatial resolution, at least as small as a few tens of nanometers. Electron energy loss spectroscopy (EELS) may be a suitable tool for this purpose, because it probes the local chemical environments around the associated elements on a nanometer scale. EELS also allows the spatial distributions of these chemical states to be visualized as a two-dimensional (2D) map by scanning the fine electron probe over a wide area of the sample, collecting spectra from many locations.

In Part I of this series of reports,[18] we showed experimentally that the degradation of the positive electrode is primarily responsible for the capacity fading at 80°C. Further quantitative analysis revealed a strong positive correlation between the degradation of the positive electrode and the quantity of inactive Ni ions produced in the active component material during the cyclic testing. We concluded that the capacity fading is mainly caused by the formation of inactive divalent and trivalent ions, presumably associated with oxygen loss in the active materials. In the present study, we employed TEM and EELS to study in detail the spatial distribution of the secondary phase responsible for degradation during aging/cycling at elevated temperatures.

Experimental

Materials.— LiNi$_{0.8}$Co$_{0.15}$Al$_{0.05}$O$_2$ powder was synthesized by a standard coprecipitation method. The positive electrodes were fabricated from this powder, conductive artificial carbon, and polyvinylidene fluoride (PVdF) binder coated on both sides of 20 μm thick aluminum sheets. The positive electrodes were assembled into 500 mAh type cylindrical cells with graphite negative electrodes. After 500–1000 charge/discharge test cycles at 60 and 80°C,[6] the cells were disassembled to examine the degraded electrodes. The capacity and internal resistance were degraded, and detailed reports of this degradation were reported in Part I[18] and elsewhere.[6]

TEM and EELS observation.— Thin foils for TEM observation were prepared in three ways, one for plan-view and two for cross-sectional observation. For plan-view observation, the electrode sheet was punched into 3 mm diameter disks, followed by argon ion milling, first from each side separately, then from both sides after perforation to avoid leaving aluminum foil at the thinnest edge of the hole. Large thin areas containing several secondary particles were produced. For cross-sectional observation, the sheet was sectioned by an ultra-microtome or a focused ion beam (FIB) instrument. The former was used for rough observation of the entire foil thickness, when unfortunately some of the active material particles fell off.
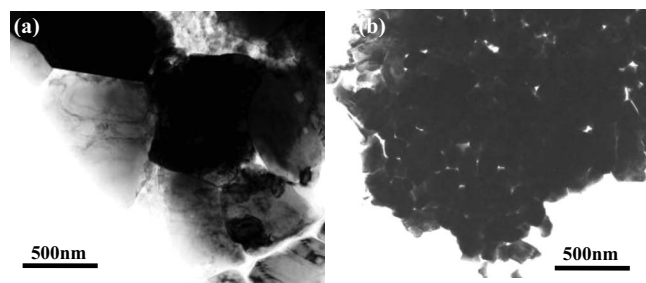
Figure 1. Representative plan-view TEM micrographs of LiNi$_{0.8}$Co$_{0.15}$Al$_{0.05}$O$_2$ positive electrodes (a) before and (b) after 1000 test cycles at 60°C.

Thin areas over an entire secondary particle (5–10 mm) were prepared by FIB to show intact surfaces at the particle edge.

Diffraction contrast images, electron diffraction patterns, and EELS were obtained by a JEM200CX TEM equipped with a Gatan Enfina 1000 spectrometer. Energy-filtering TEM (EFTEM) and electron energy loss (EEL) spectral imaging (SI), based on scanning TEM (STEM) mode, was performed using a JEM2100F TEM/STEM equipped with a Gatan Tridiem energy filter.

Multivariate analysis of SI data sets.— An STEM-SI data set consists of many EEL spectra, each instantaneously obtained from an area illuminated by the small electron probe as it scans over the region of interest (ROI) of the sample. If the ROI includes a number of different phases or different chemical states with no significant composition change, each EEL spectrum should be a linear combination of the individual EELS profiles of the constituent elements, with weights corresponding to the compositions of the different states present. Self-modeling curve resolution, or multivariate curve resolution (MCR), is a recent multivariate analysis technique which enables decomposition of such a data set into separate constituent components without requiring reference data.

In MCR, a bilinear decomposition of the SI dataset is performed using the model equation

$$D = CS^T + E \qquad [1]$$

where the dimension of the matrices are D(*NR,NC*), C(*NR,N*), S^T(*N,NC*), and E(*NR,NC*); *N* is the number of components considered; *NR* is the number of EEL spectra (number of data points obtained from the sample); *NC* is the number of channels (in the energy loss axis). D is thus a data matrix containing all SI data, C is the matrix describing how the contributions of the N components change in the *NR* rows of the data matrix (concentration profiles), and S^T is the matrix of pure spectral profiles. E is the residual matrix with the data variance or statistical noise unexplained by CS^T. The task in MCR is to find the matrices C and S^T, given the data matrix D. We adopted a modified alternating least-squares (MALS) algorithm for this purpose, because it is a fast, robust technique.[19]

## Results

TEM/EELS observation of plan-view samples.— Typical TEM images of a plan-view sample before and after 1000 cycles at 60°C are shown in Fig. 1a and b, respectively. Generally, the fabricated material became brittle compared to the original untested state, and the grains were fragmented or cracked into separate smaller particles, as shown in Fig. 1b. This is reasonable, because Li$^+$ intercalation/deintercalation during charge/discharge cycles are accompanied by repeated volume dilation and contraction.[6,13,20] As previously reported and confirmed by diffraction patterns,[15,16] some grains include a NiO-type phase. Dark-field images of the spot derived from the NiO-like phase should reveal its spatial distribution, which is shown in Fig. 2 along with a representative electron diffraction pattern. The NiO-type phase is not only localized at grain
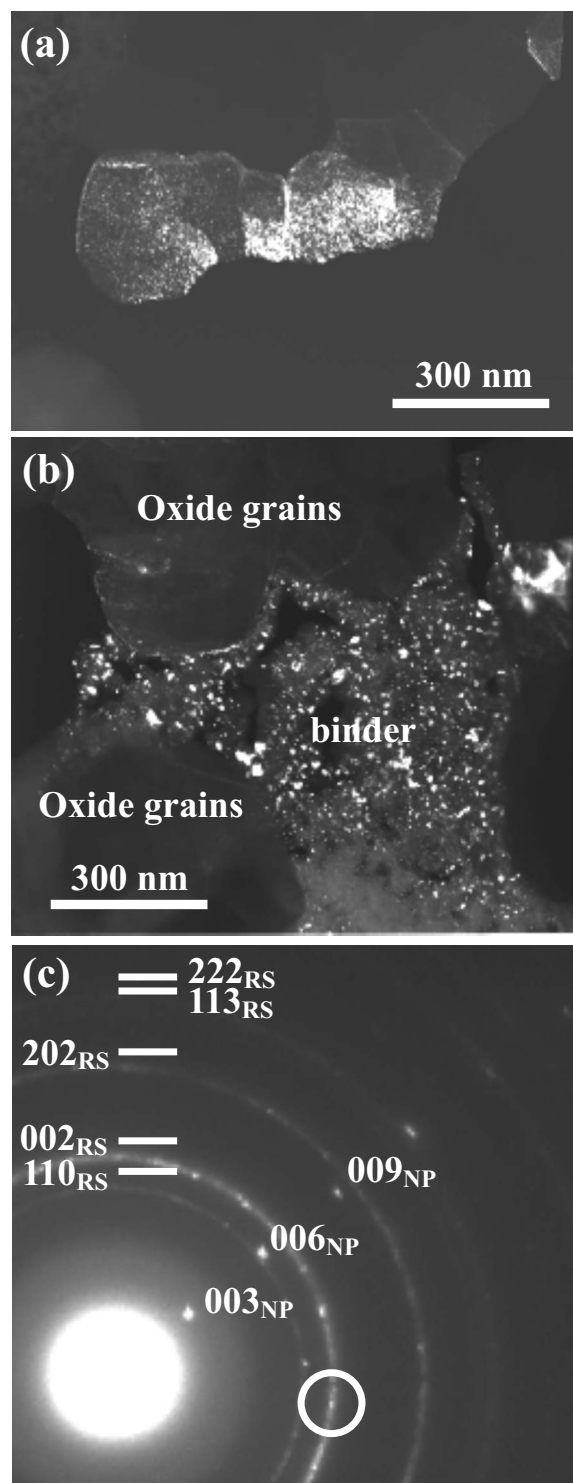
Figure 2. (a and b) Dark-field TEM images and (c) electron diffraction pattern from the cycled sample. The images are taken with the objective aperture diaphragm inserted at the encircled position in c.

boundaries but is also embedded within the grains as fine particles, as shown in Fig. 2a. This phase is sometimes also observed in the conductive carbon binder regions, as shown in Fig. 2b. Because the sample was prepared by argon ion milling, it is assumed that the fine NiO-type particles in the carbon binder regions were accidentally detached from the oxide grain surface in contact with the binder and left on the binder during ion thinning.
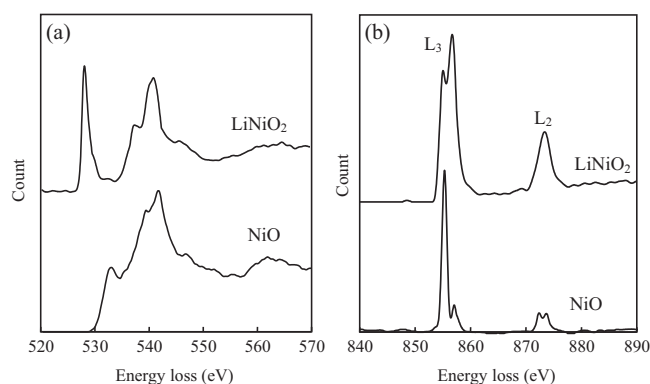
Figure 3. (a) Reference EEL spectra of oxygen K-edge and (b) nickel $L_{2,3}$-edge, taken from indicated materials.

O-K and Ni-$L_{2,3}$ reference energy-loss near-edge structure (EL-NES) spectra taken from $LiNiO_2$ and NiO powders are shown in Fig. 3a and b. It was confirmed that the initial particles exhibited the same spectral profiles as $LiNiO_2$ and the NiO-type degraded areas showed those of NiO. The Ni-$L_{2,3}$ ELNES spectra showed distinct differences in fine structures and relative intensity ratios of L_2–L_3 peaks, as shown in Table I. The L_2/L_3 intensity ratio is a good measure of the Ni valency. We tried to obtain Li-K ELNES ($\sim$58 eV) from the samples, but these overlapped the broad Co–$M_{2,3}$ spectrum and extended tail of the second plasmon. This seriously hampered any detailed analysis of the spectral fine structures of Li-K ELNES. Because the spectral acquisition areas were approximately 0.1–0.3 μm in diameter, each spectrum could be recorded from a mixture of multiple phases due to the reported size of the NiO-type phase.[15,16] The spectral features revealed are often consistent with a mixture of both phases. Note that the valency of Co is the same as that of the Ni in the same area, judging from the relative intensity ratios of L_2–L_3 peaks (not shown).

Figure 4a shows EELS of the low energy-loss region from the apparent NiO-type structures. A small 5–8 eV hump was observed at the outskirts of the elastic (zero-loss) peak. The low-loss spectrum can be compared to the joint density of states (JDOSs) with the dipole transition selection rule taken into account. JDOS was calculated based on the linearized augmented plane wave (LAPW) band method[21] for NiO and $LiNiO_2$, in which both ferromagnetic and antiferromagnetic spin configurations were considered for Ni. The calculated JDOSs, normalized by the number of cations, are shown in Fig. 4b. The JDOS of NiO increased by about 5–10 eV, which corresponds with the experimentally observed hump. This small structure is derived from a transition from the top of the valence band to the empty Ni d-band in the NiO-type structure. Ni is surrounded by six oxygen atoms in both $LiNiO_2$ and NiO structures, in which the occupancy of the d-band is similar but the number of unoccupied states per cation is larger in NiO than in $LiNiO_2$. The volume plasmon peak at 24 eV was commonly seen in both $LiNiO_2$- and NiO-type structures. These low-loss features provide another possibility for imaging the NiO-type phase; EFTEM images taken by setting a 5 eV wide energy slit at 6 and 24 eV are shown in Fig. 5a and b, respectively. Although EFTEM imaging with a low energy loss can suffer from additional diffraction contrast, the grain bound-
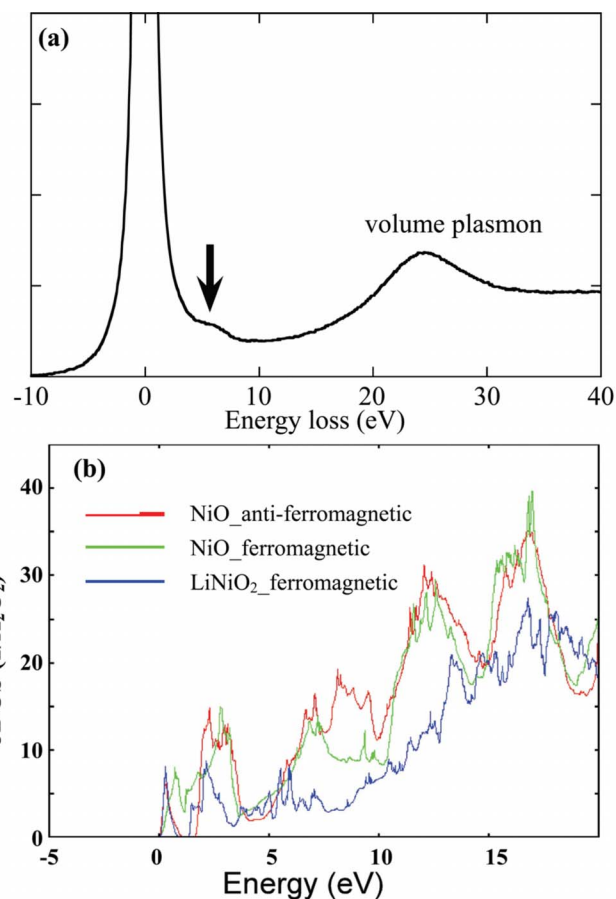

Figure 4. (Color online) (a) Low-loss spectrum from NiO. (b) JDOS calculated for NiO and $LiNiO_2$ model structures based on the LAPW band method.

aries appear bright, suggesting that NiO-type phases are localized there, as is discussed in further detail in a later section.

EFTEM of ultramicrotomy cross-sectioned sample.—Ultramicrotomy is a thin sectioning method for preparation of TEM samples, often used to prepare resin-embedded tissue. The method enables us to obtain uniform thickness over a wide area, compared to samples prepared by other thinning methods. A TEM overview of the sample after 500 test cycles at 80°C is shown in Fig. 6a. This overview was used to examine the depth dependence of the degree of degradation, from the electrode surface to the Al foil current collector interface. Of particular interest was whether there was any difference between the region near the surface, which was in contact with the electro-
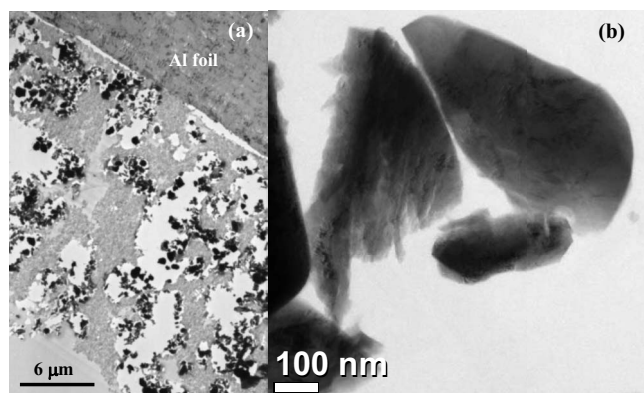
Table I. L_2/L_3 peak-area ratios of $LiNiO_2$ and NiO phases measured from EELS in Fig. 3b.

Phase	L_2/L_3
$LiNiO_2$	0.35
NiO	0.25
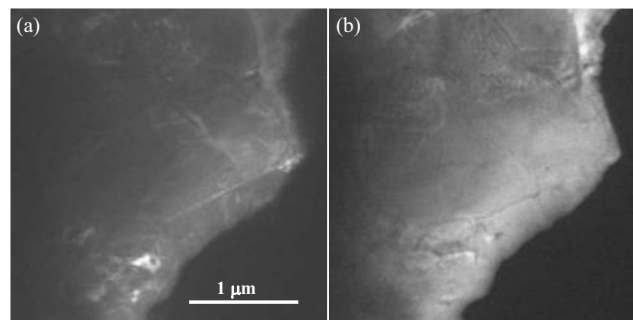
Figure 5. Energy-filtered TEM images taken with a 5 eV wide energy slit inserted at (a) 6 or (b) 23 eV.

Figure 6. (a) TEM image of ultramicrotome-sectioned positive electrode. (b) A representative oxide active material particle in (a).

Figure 8. (Color online) Images of the particles shown in Fig. 6a, processed for better visualization of the degraded regions. (a) O/Ni composition ratio map produced from EDX elemental distribution images. (b) L_2/L_3 white-line intensity ratio map of Ni from energy-filtered images. (c) Low-loss intensity ratio map from energy-filtered images. See text for details.
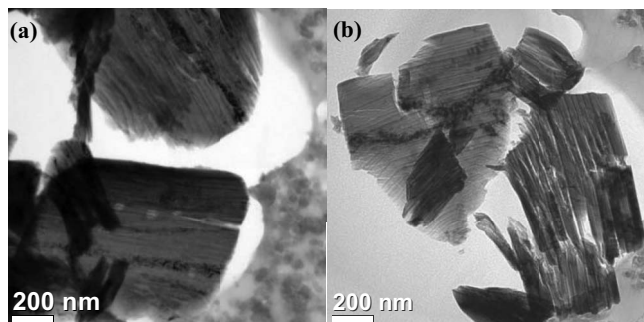
lyte, and the other regions. The open holes are due to oxide particles which fell off during sectioning. We carefully examined many particles and grains from the surface to near-substrate regions by EELS, but no noticeable general tendencies, such as that the particles near the surface include more NiO-type phase, were observed.

Sometimes we encountered fragmented grains with a comblike texture in the degraded sample, as shown in Fig. 7a and b. No similar fragmentation was observed in plan-view or FIB-sectioned samples, so it probably occurred as a result of stress concentration on mechanically fragile areas during ultramicrotomy.
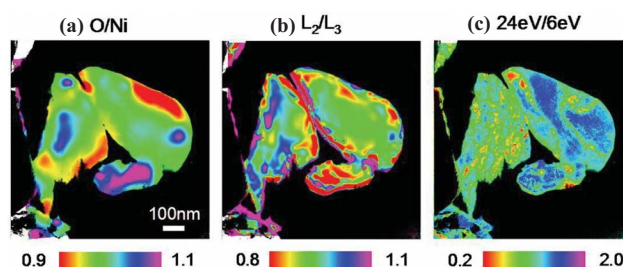
It is important to investigate local compositions to gain insight on the degradation mechanism, because the formation of an NiO-type structure requires Li deintercalation, with an accompanying reduction in oxygen content. As shown in the previous section, the NiO-type phase can be observed by dark-field imaging, but it is not possible to image all grains because of their different orientations. EFTEM is an effective alternative, because EELS is a projection of the three-dimensional structure onto the one-dimensional energy-loss axis. By selecting the spectral feature characteristic to the phase of interest, one can image all orientations of the same phase simultaneously.

A primary particle with an intact surface and minimal damage from sectioning was selected, as shown in Fig. 6b, and EFTEM images were obtained in two ways:

1. Plasmon image: Two EFTEM images were recorded by inserting a 5 eV wide energy slit at 6 and 24 eV, as discussed in the previous section. The latter image was divided by the former using an image math operation, revealing the NiO-type structure distribution.

2. Core-loss image: Ni L_2 and L_3 peaks were separately selected using a 10 eV wide slit and imaged using the three-window method to remove the background intensities. The image math operation

L_2/L_3 was also used to reveal the lower valence areas. Finally, STEM-energy dispersive X-ray analysis (EDX) elemental mapping was conducted to produce an O/Ni relative-concentration map. In order to apply these image math operations, smoothing of the image intensities was necessary, because the EFTEM images and EDX elemental distributions contained significant pixel-by-pixel intensity fluctuations. We applied the PIXON method,[22,23] one of the most effective smoothing methods, to remove statistically random noise with minimal information loss.

Each technique has its shortcomings:

1. Plasmon imaging may suffer from additional diffraction contrast. In a locally bent sample, an area satisfying a strong Bragg condition may appear dark or bright in the plasmon image irrespective of the energy loss at the area. This is because the Bragg scattering angle of a high-energy electron is compatible with a corresponding momentum transfer in the plasmon loss region, so that elastically scattered intensities may enter the energy-selecting slit.

2. Core-loss spectral intensity strongly depends on sample thickness. The higher-energy side L_2 peak is especially sensitive; therefore, the relative intensity ratio of L_3 to L_2 may vary from location to location.

3. Elemental distributions by STEM-EDX may also suffer from artifacts of sample thickness variation. Additionally, the spatial resolution is limited by statistical noise, particularly in core-loss and EDX images.

The results of the above three methods are shown in Fig. 8a-c. Degraded areas should have a NiO-type structure, lower Ni valency, and oxygen deficiency, so highly correlated areas between all three images should be sought, because any single image contains contrast artifacts and other above-mentioned errors. After this cross-correlation, it can be reliably said that most of the degradation occurs at particle surfaces and grain-boundary regions within 50–100 nm wide.

STEM-SI of FIB cross-sectioned sample.— Spatial distribution of degraded areas by MCR.— The existence of a NiO-type degraded phase was confirmed in the preceding sections, and the degradation was found to be localized at grain surfaces and boundaries. However, one should clarify the overall distribution of degraded areas over the secondary particles in relation to the area of electrolyte contact and how these areas evolve during test cycles. We thus prepared TEM thin films using FIB of the electrodes, covering entire secondary particles, and carried out an SI technique using a scanning transmission electron microscope. STEM-SI is conducted by scanning a focused electron probe over the sample with a prespecified scan step interval, recording EEL spectra at each position. From the set of obtained spectra one can extract the spectral features of interest and display their 2D spatial distributions, the intensities of which are directly correlated to their local concentrations.
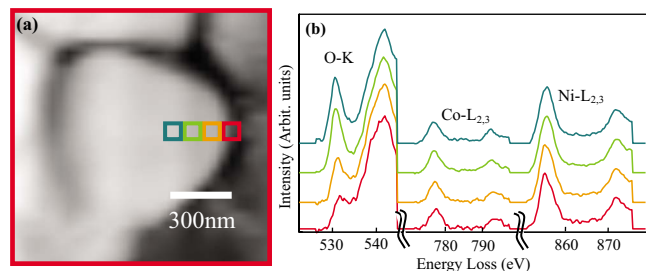
The probe size was 5 nm, scanning an area approximately 6 $\times$ 6 μm as 300 $\times$ 300 pixels with a scan step interval of

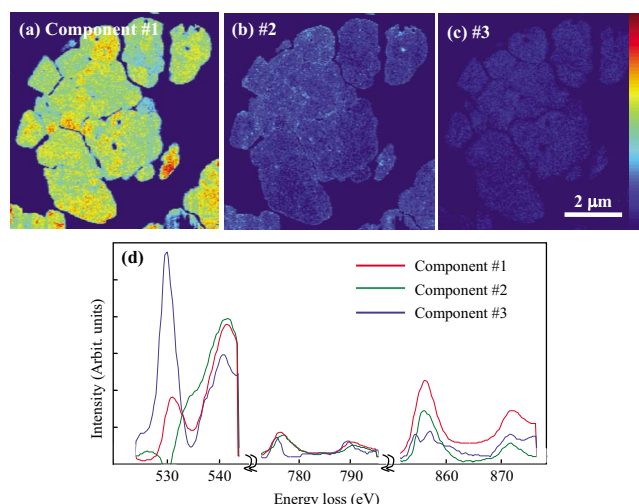**Figure 7.** Fragmented particles observed in Fig. 6a.
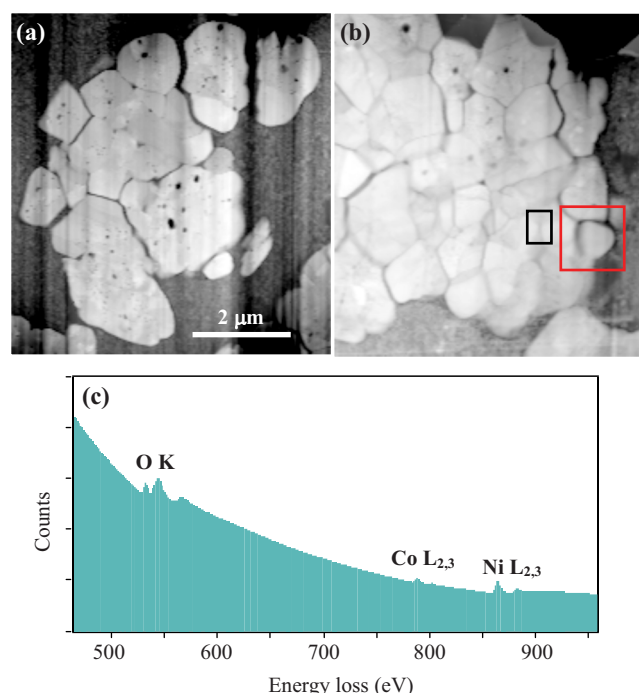
Figure 9. (Color online) Dark-field STEM images of samples (a) before and (b) after 500 test cycles at 80°C, simultaneously recorded during SI. (c) EEL spectrum extracted from the black-edged area in b.

Figure 11. (Color online) (a–c) Spatial distributions of resolved components shown in d for the sample before cycling tests. The false color indicates the local concentration corresponding to the inset color look-up table.

30–35 nm. The probe size, exposure time for each step, and step width were determined by compromise between the required spatial resolution, degree of acceptable beam damage, desired signal-to-noise ratio for each spectrum, and the total acquisition time. The energy dispersion of EELS was set to 0.3 eV/channel to cover the O-K ($\sim$525 eV), Co-$L_{2,3}$ ($\sim$793 eV), and Ni-$L_{2,3}$ ($\sim$855 eV) edges using the charge-coupled device detector with 2048 channels in the spectral dispersion direction. The duration of each spectral acquisition was 0.5 s.

Dark-field STEM images of the scanned areas simultaneously recorded in SI are shown in Fig. 9a and b for samples at the initial state and after 500 charge/discharge cycles at 80°C. The faint striations are due to nonuniform sample thickness produced by the FIB thinning procedure. The EELS spectrum from the framed area in Fig. 9b reproduced from the dataset is shown in Fig. 9c. Before processing the SI datasets, the square-framed area in Fig. 9b was picked up as shown in Fig. 10a and the corresponding O-K, Co-$L_{2,3}$, and Ni-$L_{2,3}$ ELNES spectra were extracted from several localized 2×2 pixel areas (framed from left to right in Fig. 10a), as shown respectively from top to bottom in Fig. 10b. As expected, the O-K

Figure 10. (Color online) Enlargement of the square area in Fig. 9b. O–K, Co-$L_{2,3}$, and Ni-$L_{2,3}$ ELNES spectra from top to bottom extracted from the framed areas in (a) respectively from left to right, with pre-edge background subtracted. The spectra are successively shifted vertically for better view.

ELNES profile approached that of the NiO-like phase, and the L_2-to-L_3 ratio of Ni $L_{2,3}$ white-line is reduced, consistent with Ni^{2+} from the inner-grain area to the particle edge. Hence, the SI datasets do include information on the spatial changes in ELNES spectra.

To map the NiO-type structure and other unknown phase (if any) distributions, we applied an MCR technique based on the MALS algorithm to the SI datasets.[19] It was crucial for this analysis to determine the number of components (different phases) included in the dataset. We first applied a primary component analysis (PCA) to the data, which indicated only a single significant component. This means that PCA is not able to distinguish the subtle spectral changes present, and thus the number of significant components was determined by trial and error, examining whether the resolved spectral component could be interpreted as physically meaningful.

To increase the reliability of the MCR, the spectral regions of O-K, Co $L_{2,3}$, and Ni $L_{2,3}$ to be analyzed were selected as shown in Fig. 10b. After subtracting the pre-edge background from each edge, specific energy ranges were picked up: 500–570 eV for O-K-edge, and white-line peaks for Co and Ni $L_{2,3}$-edges, or 270 channels in total. A higher-energy region of O-K ELNES was deliberately omitted, because the intensities in this region depend sensitively on sample thickness due to multiple losses. Furthermore, the carbon binder region surrounding the oxide particle was carefully removed by applying the mask, because the region was found to contain oxygen and exhibit an ELNES profile similar to the degraded phase in the oxide particle, seriously affecting the curve-resolution results. In order to minimize the rotational ambiguities of the MCR solution, a non-negativity constraint for both the spectral and concentration matrices and a normalization constraint for each row of the spectral matrix (pure spectral profile) were imposed. For the latter constraint, the 1-norm ($\Sigma_i |x_i|$) instead of the Euclidian length (2-norm) was adopted, because the spectral intensity of an element corresponds to the cross section for the core loss. Normalization by the 1-norm of each spectral profile under a non-negativity constraint allowed direct interpretation of the concentration profile as the relative concentration of each component.

MCR was applied to the present datasets by assuming two, three, and four components, but resolution into four components was found to be irrelevant because the fourth component looks like residual noise rather than a meaningful spectrum. The spatial distributions of each resolved component are shown in Fig. 11a-c for the initial state and Fig. 12a-c for samples after 500 cycles at 80°C, assuming three components are present. The pure spectral profiles
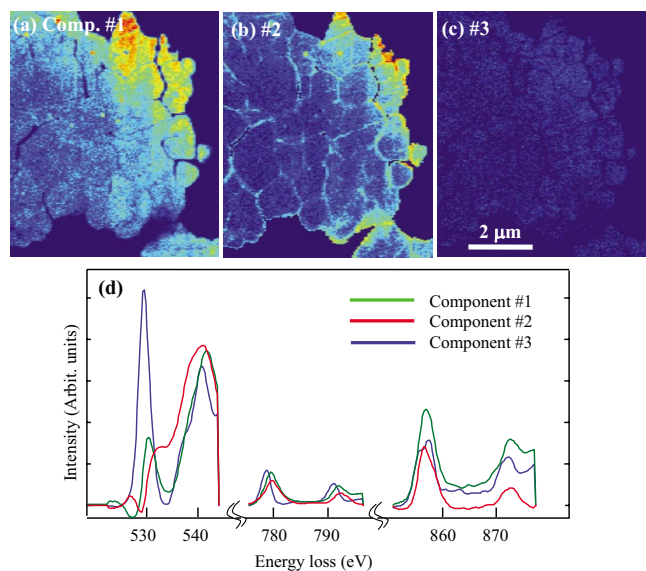
Figure 12. (Color online) (a–c) Spatial distributions of resolved components shown in d for the sample after 500 test cycles at 80°C.

Figure 13. (Color online) Spatial distribution of NiO-type phase (a) before and (b) after 500 test cycles at 80°C (c) was reproduced from Fig. 11b and 12b, with enhanced contrast. b and d are fluorine distributions in the corresponding samples on the left.
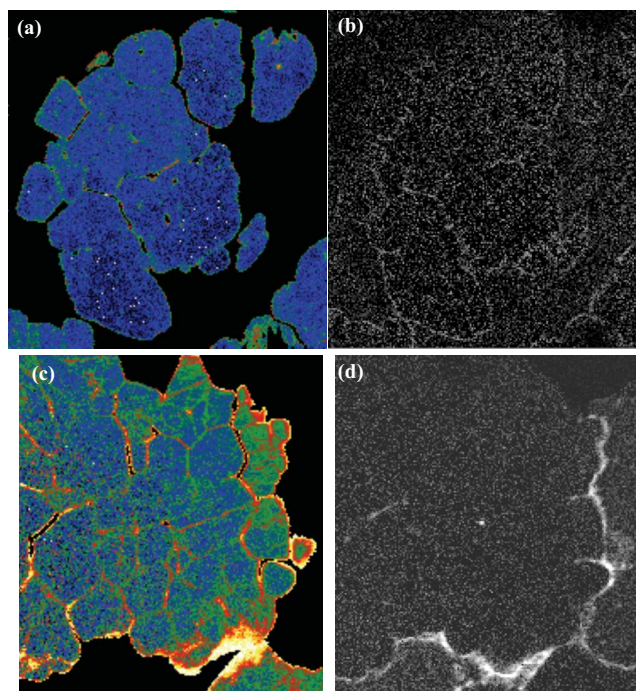
are shown in Fig. 11d and 12d. The total concentrations of the three components were calculated from the concentration matrix and are listed in Table II.

Note that the spectral profiles of the three components, particularly of the O-K-edge, are all common to two separate measurements on different samples, which increases the reliability of the results. The Ni and Co $L_{2,3}$-edges in Fig. 11d may seem distorted because the fraction of this component is small and therefore strongly affected by residual noise. It is apparent from the O-K ELNES spectral features shown in Fig. 3a that components 1 and 2 correspond to the original layered phase and a degraded NiO-type phase, respectively. This assignment is further reinforced by the fact that the associated Co- and Ni-$L_{2,3}$ ELNES show trivalent and divalent white-line intensity ratios, as shown in Fig. 3b. The O-K ELNES of component 3 is characterized by a large prepeak and can be assigned to a Li-deficient phase by comparing it to the reported spectra from $Li_{1-x}Ni_{0.8}Co_{0.2}O_2$ ($x = 0.07$–0.74).[24] The L_3/L_2 ratio of component 3 shows a value larger than that of the trivalent phase, further confirming the assignment. According to the relative prepeak intensities reported in Ref. 20, x (the fraction of Li deintercalation) ≈ 0 for component 1 and $x > 0.7$ for component 3. It is thus reasonable to conclude that a linear combination of x values in components 1 and 3, weighted by the local concentrations, provides the Li composition at each position.

Figures 11a-c and Table II show that at the initial state a significant amount of NiO-type phase already existed, particularly at the edge of the grains, and the lithium content was not deficient within the present detectable limit and spatial resolution. After 500 cycles at 80°C, the NiO-type phase was considerably increased at the grain

surfaces and boundaries, and Li was deficient at some locations. The thickness and amount of the degraded phase were consistent with the values reported in a previous section.

Fluorine distribution.— Figures 13b and d show the fluorine distributions of the initial state and after 500 test cycles, according to the conventional SI method with the pre-edge background subtracted, together with the NiO-type phase distributions of the corresponding samples (Fig. 13a and c), reproduced from Fig. 11b and 12b but with enhanced contrast for easier comparison. In Fig. 13b small amounts of fluorine were mainly distributed along the grain boundaries of the primary particles. These were likely derived from the $LiPF_6$ electrolyte rather than from the PVdF binder, because PVdF should always be detected together with the artificial carbon conductor. Fluorine was also detected at cracked particle surfaces, which suggests that the electrolyte invaded into the cracked gaps, allowing these newly formed surfaces to act as charge/discharge reaction surfaces. This is quite reasonable, because the NiO-type degraded phase was also distributed along the cracked particle surfaces in the sample after 500 test cycles, as shown in Fig. 13c, which presents strong evidence that the degradation starts at the surfaces in contact with the electrolyte.

After 500 test cycles at 80°C (Fig. 10d), significant amounts of fluorinate were distributed at the secondary particle surface. These may be the LiF precipitates reported by several other research groups,[25,26] though these precipitates would play only a minor role in electrochemical cell degradation. Notably, the NiO-type phase did not always exist near these fluorinate distributions.

Discussion

In this section, we discuss the degradation mechanism of the positive electrode active material based on the results presented above and in Part I.[18]

In Part I, we claimed that the capacity fading of the positive electrodes is mainly a result of the formation of inactive divalent [Ni(II)] and trivalent [Ni(III)] Ni ions. In the present study, the NiO-type phase [Ni(II)] evolved during cycling at elevated temperatures

Table II. Component concentrations in each sample, derived from MCR analysis of STEM-SI datasets, as shown in Fig. 11 and 12.

Sample	Normal phase (Camp. 1) (%)	NiO-type phase (Comp. 2) (%)	Li-deficient phase (Comp 3) (%)
Initial	80	18	1
After 500 test cycles	45	37	18

Sample	Normal Ni (III) (%)	Ni (II) (%)	Inactive Ni (III) (%)
Initial	89	10	1
After 500 test cycles	55	23	22

and can be produced by the reaction between a primary/secondary particle surface and the electrolyte, while inactive Ni(III) is attributable to the Li-deficient areas distributed over entire particles. Assuming that inactive Ni(II) and Ni(III) are derived from NiO-type and NiO_2-like Li-deficient phases, respectively, the concentrations of Ni ions in the different states can be estimated from Table II, the results of which are tabulated in Table III. The Ni(II) increased by 13%, consistent with the value estimated in Part I, whereas the increase in inactive Ni(III) was doubly overestimated compared to Table III in Part I. It thus appears that concentration of the Li-deficient phase does not directly correspond to the fraction of inactive Ni(III) formed.

To examine the correlation between the spatial distributions of the assumed inactive phases and oxygen concentration, EDX elemental analysis was performed, with results shown in Fig. 14. The oxygen-deficient areas roughly show a positive correlation with the spatial distribution of NiO-type phase but no appreciable correlation with the Li-deficient areas. It is therefore likely that the NiO-type phase was formed by deintercalation of Li and subsequent oxygen loss; however, the origin of the inactive Ni(III) remains unclear.

Conclusion

The microstructure of the active positive electrode material $LiNi_{0.8}Co_{0.15}Al_{0.05}O_2$ for lithium-ion secondary batteries after charge–discharge test cycles at elevated temperatures was examined in detail by means of TEM and spectroscopy. The main results obtained are summarized below:

1. NiO-type phase was found in both initial and cycled samples. This phase was significantly increased at grain surfaces and grain boundaries in the primary/secondary particles and ranged over 100 nm from the surface.

2. Li-deficient areas were also formed in the cycled samples and are presumed to be the origin of inactive Ni(III) found in Part I.[18]

3. There was no significant difference in degraded structures of active material particles from locations ranging from the surface to the Al foil collector.
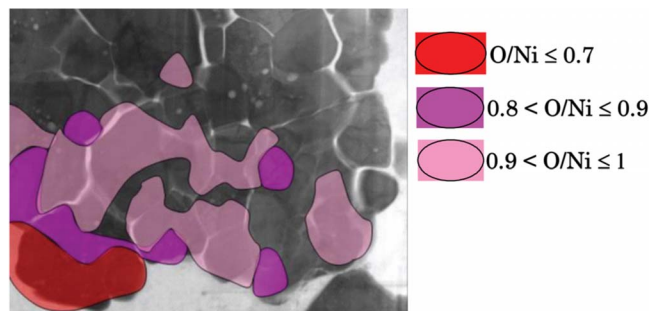
Figure 14. (Color online) Summary of EDX point-to-point elemental analysis of the degraded sample after 500 cycles at 80°C (lower half area of Fig. 9b). The O-deficient areas relative to Ni contents are shown.

4. The increase in the NiO-type phase was consistent with the formation of inactive Ni(II) described in Part I, whereas the concentration of Li-deficient areas was not in agreement with the amount of inactive Ni(III).

3. Oxygen-deficient areas showed a positive correlation with the spatial distribution of the NiO-type phase. This implies that the NiO-type phase was formed by Li deintercalation and subsequent oxygen loss.

Further investigation of the origin of inactive Ni(III) is necessary. In addition, the chemical states of Li and their spatial distribution should be analyzed using the STEM-EELS-SI-MCR technique, which enables separation of the overlapping spectra of Li-K and Co-M absorption edges.

References

1. K. Sakai, H. Azuma, A. Omaru, and S. Fujita, *J. Power Sources*, **43**, 241 (1993).
2. C. Delmas, M. Menetrier, L. Croguennec, I. Saadoune, A. Rougier, C. Pouillerie, G. Prado, M. Grune, and L. Fournès, *Electrochim. Acta*, **45**, 243 (1999).
3. T. Ohzuku, A. Ueda, and M. Kouguchi, *J. Electrochem. Soc.*, **142**, 4033 (1995).
4. S. Madhavi, G. V. Subba Rao, B. V. R. Chowdari, and S. F. Y. Li, *J. Power Sources*, **93**, 156 (2001).
5. C. H. Chen, J. Liu, M. E. Stoll, G. Henriksen, D. R. Vissers, and K. Amine, *J. Power Sources*, **128**, 278 (2004).
6. Y. Itou and Y. Ukyo, *J. Power Sources*, **146**, 39 (2005).
7. P. Arora, R. E. White, and M. Doyle, *J. Electrochem. Soc.*, **145**, 3647 (1998).
8. D. P. Abraham, S. D. Poppen, A. N. Jansen, J. Liu, and D. W. Dees, *Electrochim. Acta*, **49**, 4763 (2004).
9. R. Kostecki and F. McLarnon, *Electrochem. Solid-State Lett.*, **5**, A164 (2002).
10. R. Premanand, A. Durairajan, B. Haran, R. White, and B. Popov, *J. Electrochem. Soc.*, **149**, A54 (2002).
11. FY 2005 Annual Progress Report for Energy Storage Research and Development, http://www1.eere.energy.gov/vehiclesandfuels/pdfs/program/2005_energy_storage.pdf.
12. J. Shim, R. Kostecki, T. Richardson, X. Song, and K. A. Striebel, *J. Power Sources*, **112**, 222 (2002).
13. K. Nikolowski, N. N. Bramnik, C. Baehtz, H. Ehrenberg, and H. Fuess, *J. Power Sources*, **174**, 818 (2007).
14. Y. Uchimoto, H. Sawada, and T. Yao, *J. Power Sources*, **97–98**, 326 (2001).
15. D. P. Abraham, R. D. Twesten, M. Balasubramanian, I. Petrov, J. McBreen, and K. Amine, *Electrochem. Commun.*, **4**, 620 (2002).
16. D. P. Abraham, R. D. Twesten, M. Balasubramanian, J. Kropf, D. Fischer, J. McBreen, I. Petrov, and K. Amine, *J. Electrochem. Soc.*, **150**, A1450 (2003).
17. K. A. Striebel, J. Shim, E. J. Cairns, R. Kostecki, Y.-J. Lee, J. Reimer, T. J. Richardson, P. N. Ross, X. Song, and G. V. Zhuang, *J. Electrochem. Soc.*, **151**, A857 (2004).
18. T. Sasaki, T. Nonaka, H. Oka, C. Okuda, Y. Itou, Y. Kondo, Y. Takeuchi, Y. Ukyo, K. Tatsumi, and S. Muto, *J. Electrochem. Soc.*, **156**, A289 (2009).
19. J.-H. Wang, P. K. Hopke, T. M. Hancewicz, and S. L. Zhang, *Anal. Chim. Acta*, **476**, 93 (2003).
20. K. Dokko, M. Nishizawa, S. Horikoshi, T. Itoh, M. Mahamedi, and I. Uchida, *Electrochem. Solid-State Lett.*, **3**, 125 (2000).
21. P. Blaha, K. Schwarz, G. K. H. Madsen, D. Kvasnicka, and J. Luitz, *WIEN2K, An Augmented Plane Wave + Local Orbitals Program for Calculating Crystal Properties*, K. Schwarz and T. U. Wien, Editors, Austria (2001).
22. R. C. Puetter, T. R. Gosnell, and A. Yahil, *Annu. Rev. Astron. Astrophys.*, **43**, 139 (2005).
23. S. Muto, R. C. Puetter, and K. Tatsumi, *J. Electron Microsc.*, **55**, 215 (2006).
24. J. Graetz, C. C. Ahn, R. Yazami, and B. Fulz, *J. Phys. Chem. B*, **107**, 2887 (2003).
25. A. M. Andersson, D. P. Abraham, R. Haasch, S. MacLaren, J. Liu, and K. Aminea, *J. Electrochem. Soc.*, **149**, A1358 (2002).
26. M. Shikano, H. Kobayashi, S. Koikea, H. Sakaebe, E. Ikenaga, K. Kobayashi, and K. Tatsumi, *J. Power Sources*, **174**, 795 (2007).